Published in final edited form as:
Neuroimage. 2012 January 16; 59(2): 1290–1298. doi:10.1016/j.neuroimage.2011.07.096.

3D Fiber Tractography with Susceptibility Tensor Imaging

Chunlei Liu[1,2], **Wei Li**[1], **Bing Wu**[1], **Yi Jiang**[3], and **G. Allan Johnson**[3]

[1]Brain Imaging and Analysis Center, School of Medicine, Duke University, 2424 Erwin Rod, Suite 501, Durham, NC 27705, USA

[2]Department of Radiology, School of Medicine, Duke University, Durham, NC 27705, USA

[3]Center for In Vivo Microscopy, Duke University Medical Center, Durham, NC 27710

Abstract

Gradient-echo MRI has revealed anisotropic magnetic susceptibility in the brain white matter. This magnetic susceptibility anisotropy can be measured and characterized with susceptibility tensor imaging (STI). In this study, a method of fiber tractography based on STI is proposed and demonstrated in the mouse brain. STI experiments of perfusion-fixed mouse brains were conducted at 7.0 T. The magnetic susceptibility tensor was calculated for each voxel with regularization and decomposed into its eigensystem. The major eigenvector is found to be aligned with the underlying fiber orientation. Following the orientation of the major eigenvector, we are able to map distinctive fiber pathways in 3D. As a comparison, diffusion tensor imaging (DTI) and DTI fiber tractography were also conducted on the same specimens. The relationship between STI and DTI fiber tracts was explored with similarities and differences identified. It is anticipated that the proposed method of STI tractography may provide a new way to study white matter fiber architecture. As STI tractography is based on physical principles that are fundamentally different from DTI, it may also be valuable for the ongoing validation of DTI tractography.

Keywords

susceptibility tensor imaging; tractography; magnetic susceptibility anisotropy; phase imaging; diffusion tensor imaging

Introduction

The central nervous system (CNS) of vertebrates is composed of a massive number of neurons that are interconnected by long projection axons. Groups of closely packed axons form anatomically and functionally distinctive fiber pathways. Knowledge of these pathways allows us to examine the functional and structural connectivity between different brain anatomical regions. Determining the architecture of those fiber pathways noninvasively is, therefore, of great importance in neuroscience and medicine. Advances in diffusion tensor imaging (DTI) have made magnetic resonance imaging (MRI) the only imaging modality capable of noninvasively visualizing 3D neural fiber pathways *in vivo*

Correspondence Address: Chunlei Liu, Ph.D., Brain Imaging and Analysis Center, Duke University School of Medicine, 2424 Erwin Road, Suite 501, Campus Box 2737, Durham, NC 27705, Phone: (919)681 4788, Fax: (919)681 7033, chunlei.liu@duke.edu.

(Basser et al., 1994; Basser et al., 2000; Conturo et al., 1999; Mori et al., 1999; Moseley et al., 1990). The resulting structural connectivity has provided valuable information regarding white matter micro-architecture. After a decade-long development, DTI tractography has become a powerful tool for the characterization and diagnosis of various white matter diseases in which functional abnormalities are due to white matter structural malformations or degeneration. The biophysical basis of DTI-based fiber tracking is the anisotropic diffusion of water molecules in the highly aligned white matter fibers. It is conceivable that other MRI measurable anisotropic quantities of white matter may also allow for the tracking of fiber pathways. In fact, such alternative methods of fiber tracking are needed to complement and further validate the results of DTI tractography.

A promising candidate for alternative tractography is the anisotropic magnetic susceptibility of ordered biological structures. Recent developments of ultra-high field (7T and above) gradient-echo imaging have shown that the spatial variation of magnetic susceptibility in brain tissues can generate a unique phase contrast between gray and white matter, with superior contrast-to-noise ratio (CNR) compared to the corresponding magnitude image (Duyn et al., 2007). Based on this phase contrast, it has been reasoned that the resonance frequency shift is orientation dependent in the white matter (He and Yablonskiy, 2009). It is further discovered that the magnetic susceptibility itself is dependent on the white matter fiber orientation, as observed in a recent study of intact brains of mice (Liu, 2010). This phenomenon has also been observed in segments of human brain specimens (Lee et al., 2010), and in human brain *in vivo* (Li et al., 2011b). A method of susceptibility tensor imaging (STI) has been proposed to measure and characterize the anisotropy of magnetic susceptibility (Liu, 2010). Our most recent data indicate that white-matter susceptibility anisotropy likely arises from the anisotropic alignment of molecules in the myelin sheath. Both theoretical modeling and experimental data showed that the magnetic susceptibility of white matter decreases monotonically (becomes more diamagnetic) with increasing angle between the white matter fiber and the applied field, following a simple sine squared relationship. In other words, the largest magnetic susceptibility (least diamagnetic) is found when the fiber is aligned with the applied magnetic field. The distribution of bulk susceptibility anisotropy along the white matter reveals a simple magnetic order beneath the incredibly complex neural tissues. An immediate implication of this spatial order is that the long-range coherence in the principal susceptibility axis can be used to trace the direction of these fiber pathways.

In this study, we propose a method of fiber tractography based on STI and demonstrate the tracking of the 3D white matter fiber pathways in *ex vivo* mouse brains. Susceptibility tensors are first determined using resonance frequency shifts measured at different brain orientations with respect to the main magnetic field. To improve the accuracy, a tensor regularization method is proposed and implemented. The tensor is then decomposed in its eigensystem that is independent of the choice of coordinate system. White matter fiber pathways are reconstructed by navigating through the vector field defined by the least diamagnetic susceptibility eigenvector. While differences exist between STI- and DTI-defined fiber tracts, a high level of similarity is demonstrated in tracks of major white matter fiber bundles.

Methods

Mouse Brain MR Imaging

Proton MRI experiments on perfusion fixed mouse brains were conducted as described previously (Liu, 2010). Briefly, adult C57BL/6 mouse (n = 3, The Jackson Laboratory, Bar Harbor, ME) brains were imaged in a 21-cm-bore 7.0 T magnet interfaced to a GE Excite console modified for small animal imaging. The system provides maximal gradient strength

at 770 mT/m. Mice were anesthetized with Nembutal. A catheter was inserted into the left ventricle of the mouse heart. The animal was perfused with a peristaltic pump first with a mixture of 0.9% saline and ProHance (10:1, v:v) (Bracco Diagnostics, Princeton, NJ), then followed by a mixture of 10% buffered formalin and ProHance (10:1, v:v) (Johnson et al., 2002). As described by Johnson et al, this perfusion method simultaneously fixes the tissue while preferentially reducing the T1 relaxation time (Johnson et al., 2002). The perfused mouse brain was surgically separated from the body, but was kept within the cranium to prevent any potential damage to the brain caused by surgical removal. The specimen was sealed tightly inside a cylindrical tube (length 30 mm and diameter 11 mm). To allow free rotation, the tube was contained within and taped to a hollow sphere (diameter 30 mm). The sphere containing the specimen was placed inside a dual-channel mouse coil (diameter 30 mm, M2M imaging Corp, Cleveland OH) and scanned using a 3D spoiled-gradient-recalled-echo (SPGR) sequence with the following parameters: FOV = 22×22×22 mm^3, matrix = 256×256×256, TE = 8.0 ms, TR = 50 ms, flip angle = 60° and NEX = 1. The total acquisition time was 55 minutes per imaging volume. After each acquisition, the sphere was rotated to a different orientation and the acquisition was repeated. A total of 15 to 19 orientations were sampled that roughly cover the spherical surface evenly.

DTI images were acquired with a 3D spin-echo sequence with the same spatial resolution but reduced matrix size (256×128×128). One image volume was acquired without diffusion weighting. A total of six diffusion encoding directions were used with a b-value of 1500 s/mm^2 to allow the calculation of the diffusion tensor. The encoding directions were (1 0 1), (1 0 -1), (1 1 0), (1 -1 0), (0 1 1) and (0, 1 -1). The image acquisition time was 27 min per imaging volume. All experiments were approved by our Institutional Animal Care and Use Committee.

Susceptibility Tensor Model

According to Liu (Liu, 2010), the resonance frequency shift (Δf) of each voxel is related to the spatially distributed macroscopic susceptibility tensors as

$$\Delta f = FT^{-1}\left[\frac{1}{3}\widehat{\mathbf{H}}^{\mathrm{T}}FT(\chi)\widehat{\mathbf{H}} - \mathbf{k}^{\mathrm{T}}\widehat{\mathbf{H}}\frac{\mathbf{k}^{\mathrm{T}}FT(\chi)\widehat{\mathbf{H}}}{k^2}\right]\gamma\mu_0 H_0. \quad [1]$$

Here, FT (FT^{-1}) is the Fourier transform (inverse Fourier transform), $\hat{\mathbf{H}}$ is the unit directional vector of the applied magnetic field, $\mathbf{k}$ is the spatial frequency vector, γ is the gyromagnetic ratio of water proton, H_0 is the magnitude of the applied magnetic field, and χ is the second-order (or rank-2) susceptibility tensor.

There are six unknowns for the rank-2 susceptibility tensor assuming symmetry. To facilitate the calculation of the susceptibility tensor, Eq. [1] is reformulated as follows:

$$\boldsymbol{\delta}(\mathbf{k}) = a_{11}\boldsymbol{\chi}_{11}(\mathbf{k}) + a_{12}\boldsymbol{\chi}_{12}(\mathbf{k}) + a_{13}\boldsymbol{\chi}_{13}(\mathbf{k}) + a_{22}\boldsymbol{\chi}_{22}(\mathbf{k}) + a_{23}\boldsymbol{\chi}_{23}(\mathbf{k}) + a_{33}\boldsymbol{\chi}_{33}(\mathbf{k}) \quad [2]$$

Here, $\boldsymbol{\delta}(\mathbf{k})$ is the 3D Fourier transform of $\Delta f / \gamma \mu_0 H_0$ and $\boldsymbol{\chi}_{ij}(\mathbf{k})$ is the 3D Fourier transform of susceptibility tensor element χ_{ij}. The coefficient, a_{ij}, is defined as

$$\begin{aligned} a_{ij} &= \tfrac{1}{3}H_iH_i - \mathbf{k}^{\mathrm{T}}\widehat{\mathbf{H}}\tfrac{k_iH_i}{k^2} \quad (i=j) \\ a_{ij} &= \tfrac{2}{3}H_iH_j - \mathbf{k}^{\mathrm{T}}\widehat{\mathbf{H}}\tfrac{k_iH_j+k_jH_i}{k^2} \quad (i \neq j) \end{aligned} \quad [3]$$

In principle, a minimum of six non-collinear measurements are required to solve Eq. [2] for $\boldsymbol{\chi}$. Given N set of data measurements in this study, the susceptibility tensor can be estimated by solving the following system of linear equations formed by stacking N sets of Eq. [2] in the format of matrix-vector multiplication

$$\boldsymbol{\delta}=\mathbf{A}\boldsymbol{\chi}. \quad [4]$$

Here, $\boldsymbol{\delta}$ is formed by stacking the N measurement of $\delta(\mathbf{k})$ in an $N \times 1$ vector; A is an $N \times 6$ matrix whose elements are a_{ij}; $\boldsymbol{\chi}$ is a 6×1 vector of χ_{ij}.

To evaluate the conditioning of the matrix inversion, we selected 6 orientations out of the N directions with angles reasonably well separated to solve Eq. [4] (repeated 3 times). The calculated condition number of $\boldsymbol{A}$ is always smaller than 34 for all three trials, suggesting that 6 independent measurements would be sufficient to ensure the conditioning of the inversion of Eq. [4] (Supplementary materials). Since this study aims at demonstrating the feasibility of STI based tractography, a large number of independent measurements are used to improve the SNR and accuracy of the susceptibility tensor quantification without further optimization of the orientation sampling.

Data Analysis

The complex gradient echo images were separated into magnitude and phase. The magnitude image was used to extract the brain tissue using ITK-SNAP (Yushkevich et al., 2006). The magnitude images were linearly registered to the DTI images using FSL-FLIRT (FMRIB, Oxford University). The phase from the gradient echo images was unwrapped with the Laplacian based phase unwrapping method (Li et al., 2011b; Schofield and Zhu, 2003). The transformation matrix obtained from the linear registration was used to register the unwrapped phase to the DTI volumes. The background component of the unwrapped phase that originates from sources outside the brain was removed by sphere mean value filtering with varying diameters (Li et al., 2011b; Schweser et al., 2011b).

Calculation of apparent magnetic susceptibility—Apparent magnetic susceptibility was determined for each phase map with the LSQR algorithm as described previously (Li et al., 2011b), other reported methods may be seen in (de Rochefort et al., 2010; Li et al., 2011b; Marques and Bowtell, 2005; Salomir R, 2003; Schweser et al., 2010; Wharton and Bowtell, 2010). If we assume that the major eigenvector of susceptibility tensor lies along the fiber direction, it can be shown, by susceptibility tensor rotation and projection, that the relationship between magnetic susceptibility and fiber angle follows the following equation:

$$\Delta\chi=\Delta\chi_{\max}\sin^2\alpha+\Delta\chi_0. \quad [5]$$

Here, $\Delta\chi$ is the magnetic susceptibility of the white matter in reference to surrounding gray matter (the average value of all 5 red regions of interest in Fig. 1); $\Delta\chi_0$ is a baseline isotropic susceptibility difference, $\Delta\chi_{\max}$ is the anisotropic susceptibility difference, and the **fiber angle** α is defined as the angle between the fiber direction and the main magnetic field direction.

Calculation of magnetic susceptibility tensor with regularization—Magnetic susceptibility tensors were determined voxel-by-voxel by solving Eq. [4] in the **k**-space in the subject's frame of reference. As images acquired at different orientations have different deformation due to the field effects, even though they are registered, imperfection in the registration causes inaccurate estimation of the susceptibility tensor. The error is especially

severe at tissue boundaries where there is a rapid change of susceptibility, resulting in erroneous anisotropy. To reduce this error, we constrain the spatial variation of susceptibility anisotropy to be characterized by low spatial frequencies, while the susceptibility of high spatial frequencies components (i.e. at the outer k-space) is relatively isotropic. Analytically, this constraint imposed at the peripheral k-space can be expressed as

$$\begin{aligned}\boldsymbol{\chi}_{11}(\mathbf{k}) &\approx \boldsymbol{\chi}_{22}(\mathbf{k}) \approx \boldsymbol{\chi}_{33}(\mathbf{k})\\ \boldsymbol{\chi}_{12}(\mathbf{k}) &\approx \boldsymbol{\chi}_{13}(\mathbf{k}) \approx \boldsymbol{\chi}_{23}(\mathbf{k}).\end{aligned} \quad [6]$$

This is implemented as a regularization term to Eq. [4] with a weighting function, $W(k)$, defined by the Fermi filter as

$$W(k)=1-\{1+\exp[(k-\alpha)/\beta]\}^{-1}, \quad [7]$$

Where the width (α) and transition width (β) have the same unit as k. α is adjusted according to the degree of misregistration: the higher level of misregistration there is, the smaller α should be. β is adjusted to ensure a reasonably smooth transition to avoid any Gibbs ringing artifact. After extensive testing, α and β were set to $0.5k_{\max}$ and $0.06k_{\max}$, respectively, which performs well empirically. The inclusion of the regularization will give rise to blurring in the resulting susceptibility tensors. The amount blurring is determined by the filter width. Given α *of* $0.5k_{\max}$, it is estimated that the blurring will be around 2 pixels.

Given this constraint, susceptibility tensors can be estimated by solving the following regularized minimization problem

$$\min\|\boldsymbol{\delta}-\mathbf{A}\boldsymbol{\chi}\|+W(k)\begin{pmatrix}\|\chi_{11}(k)-\chi_{22}(k)\|+\|\chi_{22}(k)-\chi_{33}(k)\|+\|\chi_{11}(k)-\chi_{33}(k)\|+\\ \|\chi_{12}(k)-\chi_{13}(k)\|+\|\chi_{13}(k)-\chi_{23}(k)\|+\|\chi_{12}(k)-\chi_{23}(k)\|\end{pmatrix}. \quad [8]$$

STI tractography—The susceptibility tensor calculated from Eq. [8] is decomposed into three eigenvalues and corresponding eigenvectors. The three eigenvalues define three principal susceptibilities, χ_1, χ_2 and χ_3, ranked in a descending order. In DTI tractography, the fractional anisotropy (FA) map is used to identify regions of white matter fibers, and to set the threshold for initializing and terminating the fiber tracking procedure. Unlike DTI, the definition of susceptibility anisotropy is challenging, given the difficulties in susceptibility tensor quantification and the relative nature of susceptibility tensor values. Instead of defining a quantitative measure of susceptibility anisotropy, we used a susceptibility index ***SI*** to highlight the white matter for fiber tracking, based on the fact that white matter has anisotropic susceptibility and has the smallest susceptibility:

$$SI=(|\chi_1-\chi_3|+\gamma)/\bar{\chi}, \quad [9]$$

where $|\chi_1-\chi_3|$ is a direct measurement of susceptibility anisotropy, γ is an adjustable parameter and $\bar{\chi}$ is the mean susceptibility. Since the image quality of $|\chi_1-\chi_3|$ is usually not sufficient for fiber tracking while $\bar{\chi}$ provides excellent contrast between gray and white matter, γ and $\bar{\chi}$ are introduced to achieve a balance between characterization of susceptibility anisotropy and sufficient image quality for fiber tracking. According to Eq. [9], as γ increases, the susceptibility index, *SI*, becomes less reflective of susceptibility anisotropy and approaches the image contrast of $\gamma/\bar{\chi}$. As the dynamic range of $|\chi_1-\chi_3|$ is approximately ~0.8 ppm (see results section and Fig. 3), an empirical value of 1 ppm is chosen for γ. This

value gives approximately equal contribution for anisotropy and mean susceptibility in *SI* and it appears to be a good choice after extensive testing. In addition, to avoid dividing by zero, the reference of $\bar{\chi}$ is reset to the minimum of the mean susceptibility (~ -0.7ppm), so that all the values of $\bar{\chi}$ are positive for all tissue types. To facilitate subsequent fiber tracking, the resulting *SI* is further windowed and scaled to the range of 0 and 1 to obtain a similar contrast as FA by DTI.

Although more sophisticated tracking algorithms are conceivable to utilize the unique properties of the susceptibility tensor, existing algorithms developed in DTI (Basser et al., 2000; Mori et al., 1999) can be readily translated to STI given their common utilization of the tensor field. In the current implementation, tracking is initiated from a given voxel (or region of interest) when *SI* is above a certain level (0.35 in this study) and propagated through a continuous vector field defined by the major eigenvector that is associated with the largest principal susceptibility. Tracking is terminated when *SI* decreases to below a minimum threshold (0.35 in this study). Tracking is also terminated when the angle between two adjacent vectors is larger than a given tolerance (60°). This STI-based fiber tracking was realized with the DtiStudio (Jiang et al., 2006) (Johns Hopkins University) by substituting the diffusion tensor with the susceptibility tensor and the FA with *SI*. 3D visualization was performed in Avizo (Visualization Science Group, Inc. Burlington, MA). As a comparison, DTI-based fiber tracking was also conducted in DtiStudio with the following parameters: the FA threshold is 0.3 and the angle is less than 60°.

Results

Dependence of magnetic susceptibility on fiber orientation

For better visualization of white matter structures, we used higher image intensity to represent more diamagnetic susceptibility (being brighter), since white matter is more diamagnetic relative to gray matter. In addition, this way of susceptibility visualization is consistent with the way of displaying frequency shift in NMR spectroscopy. Figure 1A shows the apparent magnetic susceptibility at three representative orientations. It can be seen that the contrast between white matter and gray matter grows stronger as the fiber angle increases and the white matter becomes more diamagnetic (e.g. in the anterior commissure pointed by arrows). The scatter plot in Figure 1B illustrates the relationship between the apparent magnetic susceptibility and the fiber angle that is well described with the sine squared relationship shown in Eq. [5]. Importantly, the susceptibility contrast between white and gray matter reaches its minimum at 0°. In other words, the magnetic susceptibility is the least diamagnetic along the fiber direction. This relationship provides the experimental foundation for the proposed STI-based tractography.

Magnetic Susceptibility Tensor

Figure 2 shows all six elements of the susceptibility tensors of a representative slice calculated with the proposed regularization method. For isotropic susceptibility, we expect a diagonal tensor with minimal off-diagonal elements. The appearance of varying susceptibility contrast in the off-diagonal entries (χ_{12}, χ_{13} and χ_{23}) clearly shows that susceptibility in the white matter is anisotropic. For example, the hippocampal commissure appears bright in some tensor elements while dark in some other elements. Such orientation-dependent contrast mirrors the observation Moseley et al made in diffusion-weighted images of the cat brain (Beaulieu, 2002; Moseley et al., 1991). It is further seen that the susceptibility anisotropy is mostly prevalent within the white matter region and is weak in the gray matter.

Decomposition of Susceptibility Tensor

Figure 3 shows the three principal susceptibility maps from two coronal slices. These principal susceptibilities are coordinate-system independent and rotationally invariant. The three principal susceptibilities are labeled by χ_1, χ_2, and χ_3, ranked in a descending order. Since higher intensity is used to represent more diamagnetic susceptibility, maps of χ_1, χ_2, and χ_3 exhibit increasing brightness even though algebraically they have decreasing values. The different value and contrast in the three principal susceptibilities as well as the contrast in $|\chi_1 - \chi_3|$ further confirm the presence of anisotropic susceptibility in the white matter. The eigenvalue decomposition not only yields the principal susceptibility values, but also provides the tensor vector field to be used for tractography. The mean susceptibility $\bar{\chi}$, shown in the figure, is equivalent to the magnetic susceptibility determined by the multi-orientation method described previously by Liu et al (Liu et al., 2009) if the orientations are chosen properly to achieving uniform sampling.

STI Tractography

Figure 4 compares *SI* maps of STI to FA maps of DTI. Examples of *SI* are shown in Figure 4A, demonstrating that the overall contrast exhibited in the *SI* is similar to that in the FA. Figure 5 shows the corresponding color-coded *SI* or FA maps based on the direction of the major eigenvector with the following color scheme: red representing anterior-posterior, green representing left-right and blue representing dorsal-ventral. Although there are discrepancies in the color-coded anisotropy maps between STI and DTI, especially in regions of small fiber bundles, the fiber orientation are mostly consistent in major fiber bundles (arrows). Figure 4&5 illustrates that it is the principal axis that defines a well organized spatial network that runs through the white matter regions.

Figure 6 compares fiber tracts reconstructed using STI and DTI in the anterior comissure, the hipocampal commissure and the posterior corpus callosum. In all three cases, a single ROI (yellow circle in Figure 6) was drawn in the middle of each pathway to initialize the tracking procedure and the same starting and terminating criteria were used. The resulting STI fiber tracks share striking similarities with DTI in all three cases. Particularly, the smooth U-shaped anterior commissure tracks further confirm the long-range coherence of the vector field determined by STI. A voxel-by-voxel comparison of fiber orientation between DTI and STI is shown in Figure 7. Small angle differences are seen in major white matter fiber bundles (blue color) while significant differences are also present throughout the white matter. Table 1 summarizes the statistics of the selected white matter fiber bundles. In general, the two methods of fiber tracking yield comparable results for large fiber bundles with STI fibers being generally shorter. In particular, for smaller and more complicated fiber structures, DTI results longer and smoother pathways than STI.

Discussion

We have proposed and demonstrated a method of fiber tractography using STI. The tractography relies on the recently discovered anisotropic magnetic susceptibility in the white matter. High-quality susceptibility tensors were calculated with a regularized numerical algorithm. 3D fiber pathways were reconstructed by navigating through the vector field defined by the major eigenvector (corresponding to the least diamagnetic susceptibility eigenvalue) of the susceptibility tensor. The STI-based fiber tracking is compared to DTI for large white matter fiber bundles with both similarities and differences identified.

Biophysical basis of STI tractography

The basic principle of STI tractography is that the principal axis of the magnetic susceptibility anisotropy lay along the axons in the white matter fiber. This principle is

developed based on the existence of anisotropic susceptibility in the white matter and the underlying molecular arrangement around the axons. Magnetic susceptibility anisotropy differs from the commonly known orientation dependency of resonance frequency shifts. The predominant source of the orientation dependence of resonance frequency shift is the geometry of the tissue via the long-range dipolar field. Orientation-varying frequency occurs even for isotropic susceptibility. Susceptibility anisotropy in bulk tissues, on the other hand, originates from ordered microstructure (in this case the axon) and the inherent anisotropy of electron orbital magnetic moment. Although residual dipole moment exists in liquid crystals and purified protein solutions and has been used to determine molecular structures (Lohman and MacLean, 1978; Otting et al., 1991; van Zijl et al., 1984), the bulk dipole moment has long been thought to be negligible in a heterogeneous molecular environment due to fast molecular tumbling and spatial averaging. Such is the case for the gray matter where tissue structural heterogeneity is more prevalent as demonstrated by the apparent lack of susceptibility anisotropy within the gray matter.

A number of molecular sources have been proposed to interpret the phase and susceptibility contrast between gray and white matter including myelin, iron, chemical exchange and macromolecules (Haacke et al., 2007; He and Yablonskiy, 2009; Liu, 2010; Shmueli et al., 2009; Zhong et al., 2008). A recent study on the shiverer mouse mutation showed that the phase/susceptibility contrast between gray and white matter is nearly absent due to the loss of myelin sheath (Liu et al., 2011). It is hypothesized that the cylindrical arrangement of molecules with anisotropic molecular magnetic susceptibility in the myelin sheath is the origin of the observed bulk anisotropic magnetic susceptibility, which would lead to a sine squared relationship between susceptibility contrast and fiber angle. This hypothesis is well supported by the observed variations in apparent susceptibility of white matter determined at different orientations (Fig. 1). This sine squared relationship indicates that the white matter fiber is least diamagnetic along the fiber direction, which is the physical basis to perform the STI-based tractography by following the direction corresponding to the least diamagnetic susceptibility.

STI tractography vs. DTI tractography

Extensive research has been conducted over the past decade to develop DTI tractography, from improving image quality to refining tracking algorithms. Clearly, one should not expect the first attempt of STI tractography to achieve the same quality as DTI tractography. Nevertheless, similar orientations between STI fiber pathways and DTI fiber tracts were observed in major fiber bundles such as the anterior commissure, the hippocampal commissure and the posterior corpus callosum. While there is a high level of agreement in most large fiber bundles, STI tracking in small fiber bundles, and also some larger fiber bundles, such as the superior regions of corpus callosum, have shown more pronounced differences. The differences may be attributed to a number of factors. First, small fiber bundles are susceptible to imperfect linear image registration which results in inaccurate estimation of the susceptibility tensor. This is consistent with the fact that the discrepancy also is more likely to occur at the boundaries of larger fiber bundle. Second, STI-based tractography underlies a physical principle that differs fundamentally from diffusion anisotropy. It is possible that this fundamental difference may translate to different fiber tracks. We have assumed that the least diamagnetic susceptibility lies in the direction of white matter fibers. Though this assumption appears to be fully supported in the major fiber bundles, it needs to be further validated in other whiter matter regions and also *in vivo*. Clearly, more work is needed to completely understand the phenomenon of anisotropic susceptibility and to further develop the proposed tracking method. Because of their differences in the underlying mechanism, STI tractography may provide further insights on tissue microstructure that can potentially compliment the DTI tractography.

Technical considerations and advancements

When designing an STI experiment for tractography, two important factors need to be considered and optimized. First, sensitizing the effect of susceptibility relies on the accumulation of off-resonance phase which is dependent on the field strength and TE. Higher field strength and longer TE enhance the phase contrast between gray and white matter. However, longer TE also results in stronger T2* weighting and lower signal-to-noise ratio (SNR). At higher field strength, the frequency separation caused by susceptibility is increased thus allowing a shorter TE. Consequently, an optimal choice of TE may be determined by balancing out CNR and SNR at different field strength. In this study, the ProHance (gadoteridol) contrast agent was applied to allow high-resolution DTI by shortening the T1-relaxation time. It is known that ProHance does not cross intact blood-brain barrier (Bellin et al., 2003). However, it is unclear whether and where ProHance diffuses into the tissue during and after fixation, and how ProHance affects the susceptibility of gray and white matter tissue. It should be emphasized that although susceptibility anisotropy may possibly be influenced by the presence of ProHance, the anisotropy is not caused by the contrast agent. Our experimentation on specimens that were not treated with ProHance (Liu et al., 2011) and on human brains *in vivo* (Li et al., 2011b) also confirmed the existence of susceptibility anisotropy. Nevertheless, further studies are required to completely understand the effect of ProHance and other potential tissue stains.

As the susceptibility tensor contains six unknowns, a minimum of six non-collinear measurements is needed. More measurements improve the accuracy of the calculated susceptibility tensors at the expense of increasing the acquisition time. The primary challenge of *in vivo* STI tractography is the necessity of rotating a subject's head inside the scanner. In principle, orientation sampling can be accomplished more conveniently by rotating the magnetic field. However, the design of modern MRI scanner obviously precludes such experimentation. Rotating the head in a small coil is clearly not ideal. The utilization of larger head coil or body coil could allow wider range of rotations. However, the rotation angle is still limited by the physical constraints of human body. With the limited sampling angles, advanced algorithms such as the proposed regularization method for computing susceptibility tensor will be even more necessary for improved numerical stability. Although rotating the head is inconvenient, the magnetic susceptibility tensor can be measured *in vivo* in the human brain on a standard clinical 3.0 T scanner (Li et al., 2011a).

While the challenges for *in vivo* studies are significant, they are less so for magnetic resonance histology. And the potential for STI in MR histology is clear. The experiments performed here were accomplished with manual manipulation of the specimen. But automated mechanical methods would be straight forward. One could readily implement a goniometer not unlike that used routinely for electron spin resonance studies of single crystal g value anisotropy (Klette et al., 1993).

Applications and future directions

The characteristics of STI, such as high SNR, high spatial resolution and low specific-absorption rate, make it an attractive method for high resolution tensor imaging of in vivo human brain. High quality gradient-echo phase images of human brain with 500-μm isotropic resolution can be routinely acquired on standard clinical 3.0 T scanners (Schweser et al., 2011a). Higher resolution can be readily achieved at 7.0 T and higher fields (Moseley et al., 2009). The possibility of conducting fiber tracking on the human brain at these ultra-high resolutions has fascinating potential and may open new avenues for studying brain connectivity. As STI utilizes the gradient echo sequence, it is robust against B1 field imhomogeneity and does not suffer from the heating problem encountered with spin echo at

7.0 T. Further, STI is compatible with ultra-short T2 species such as macromolecules and tendons where DTI is not feasible.

Further advancement of STI tractography will benefit from faster acquisition and more robust estimation of the tensor. STI tractography can be further extended to resolve fiber crossings (Basser et al., 2000; Frank, 2001; Lin et al., 2003; Tuch et al., 2002) by incorporating multiple tensors and higher order tensors (Liu et al., 2004; Liu et al., 2010). While much more work is needed to fully realize the potential of STI and STI tractography, the immediate impact for small animal specimen imaging is clear. The improved contrast provides yet one more tool for characterizing the structure in genetic models, in disease models, and in a wide range of basic sciences. At the same time, studies in these same models will help elucidate the underlying mechanism and provide the basic underpinnings to permit translation of the technique from mouse to man.

Supplementary Material

Refer to Web version on PubMed Central for supplementary material.

Acknowledgments

The authors thank Gary Cofer, MS, and Yi Qi, MD, of Duke University Center for In Vivo Microscopy for their technical assistance. The study is supported by the National Institutes of Health (NIH) through grant R00EB007182. MRI data acquisition was conducted at the Duke Center for In Vivo Microscopy, an NCRR National Biomedical Technology Research Center (P41 RR005959) and Small Animal Imaging Resource Program (U24 CA092656). Data analysis was performed at the Brain Imaging and Analysis Center of Duke University.

References

Basser PJ, Mattiello J, LeBihan D. Estimation of the effective self-diffusion tensor from the NMR spin echo. J Magn Reson B. 1994; 103:247–254. [PubMed: 8019776]

Basser PJ, Pajevic S, Pierpaoli C, Duda J, Aldroubi A. In vivo fiber tractography using DT-MRI data. Magn Reson Med. 2000; 44:625–632. [PubMed: 11025519]

Beaulieu C. The basis of anisotropic water diffusion in the nervous system - a technical review. NMR Biomed. 2002; 15:435–455. [PubMed: 12489094]

Bellin MF, Vasile M, Morel-Precetti S. Currently used non-specific extracellular MR contrast media. European Radiology. 2003; 13:2688–2698. [PubMed: 12819914]

Conturo TE, Lori NF, Cull TS, Akbudak E, Snyder AZ, Shimony JS, McKinstry RC, Burton H, Raichle ME. Tracking neuronal fiber pathways in the living human brain. Proc Natl Acad Sci U S A. 1999; 96:10422–10427. [PubMed: 10468624]

de Rochefort L, Liu T, Kressler B, Liu J, Spincemaille P, Lebon V, Wu JL, Wang Y. Quantitative susceptibility map reconstruction from MR phase data using Bayesian regularization: validation and application to brain imaging. Magnetic Resonance in Medicine. 2010; 63:194–206. [PubMed: 19953507]

Duyn JH, van Gelderen P, Li TQ, de Zwart JA, Koretsky AP, Fukunaga M. High-field MRI of brain cortical substructure based on signal phase. Proc Natl Acad Sci U S A. 2007; 104:11796–11801. [PubMed: 17586684]

Frank LR. Anisotropy in high angular resolution diffusion-weighted MRI. Magn Reson Med. 2001; 45:935–939. [PubMed: 11378869]

Haacke EM, Ayaz M, Khan A, Manova ES, Krishnamurthy B, Gollapalli L, Ciulla C, Kim I, Petersen F, Kirsch W. Establishing a baseline phase behavior in magnetic resonance imaging to determine normal vs. abnormal iron content in the brain. J Magn Reson Imaging. 2007; 26:256–264. [PubMed: 17654738]

He X, Yablonskiy DA. Biophysical mechanisms of phase contrast in gradient echo MRI. Proc Natl Acad Sci U S A. 2009; 106:13558–13563. [PubMed: 19628691]

Jiang H, van Zijl PC, Kim J, Pearlson GD, Mori S. DtiStudio: resource program for diffusion tensor computation and fiber bundle tracking. Comput Methods Programs Biomed. 2006; 81:106–116. [PubMed: 16413083]

Johnson GA, Cofer GP, Gewalt SL, Hedlund LW. Morphologic phenotyping with MR microscopy: The visible mouse. Radiology. 2002; 222:789–793. [PubMed: 11867802]

Klette R, Toerring JT, Plato M, Moebius K, Boenigk B, Lubitz W. Determination of the g tensor of the primary donor cation radical in single crystals of Rhodobacter sphaeroides R-26 reaction centers by 3-mm high-field EPR. The Journal of Physical Chemistry. 1993; 97:2015–2020.

Lee J, Shmueli K, Fukunaga M, van Gelderen P, Merkle H, Silva AC, Duyn JH. Sensitivity of MRI resonance frequency to the orientation of brain tissue microstructure. Proc Natl Acad Sci U S A. 2010; 107:5130–5135. [PubMed: 20202922]

Li W, Wu B, Liu C. In vivo evidence of susceptibility anisotropy and susceptibility tensor imaging of human brain. Proc Int Soc Mag Res Med. 2011a

Li W, Wu B, Liu C. Quantitative susceptibility mapping of human brain reflects spatial variation in tissue composition. Neuroimage. 2011b; 55:1645–1656. [PubMed: 21224002]

Lin CP, Wedeen VJ, Chen JH, Yao C, Tseng WY. Validation of diffusion spectrum magnetic resonance imaging with manganese-enhanced rat optic tracts and ex vivo phantoms. Neuroimage. 2003; 19:482–495. [PubMed: 12880782]

Liu C. Susceptibility tensor imaging. Magn Reson Med. 2010; 63:1471–1477. [PubMed: 20512849]

Liu C, Bammer R, Acar B, Moseley ME. Characterizing non-Gaussian diffusion by using generalized diffusion tensors. Magn Reson Med. 2004; 51:924–937. [PubMed: 15122674]

Liu C, Li W, Johnson GA, Wu B. High-field (9.4T) MRI of brain dysmyelination by quantitative mapping of magnetic susceptibility. Neuroimage. 2011 In press.

Liu C, Mang SC, Moseley ME. In vivo generalized diffusion tensor imaging (GDTI) using higher-order tensors (HOT). Magn Reson Med. 2010; 63:243–252. [PubMed: 19953513]

Liu T, Spincemaille P, de Rochefort L, Kressler B, Wang Y. Calculation of Susceptibility Through Multiple Orientation Sampling (COSMOS): A Method for Conditioning the Inverse Problem From Measured Magnetic Field Map to Susceptibility Source Image in MRI. Magnetic Resonance in Medicine. 2009; 61:196–204. [PubMed: 19097205]

Lohman JAB, MacLean C. Magnetic field induced alignment effects in 2H NMR spectra. Chemical Physics Letters. 1978; 58:483–486.

Marques JP, Bowtell R. Application of a Fourier-based method for rapid calculation of field inhomogeneity due to spatial variation of magnetic susceptibility. Concepts in Magnetic Resonance Part B: Magnetic Resonance Engineering. 2005; 25B:65–78.

Mori S, Crain BJ, Chacko VP, van Zijl PC. Three-dimensional tracking of axonal projections in the brain by magnetic resonance imaging. Ann Neurol. 1999; 45:265–269. [PubMed: 9989633]

Moseley ME, Cohen Y, Kucharczyk J, Mintorovitch J, Asgari HS, Wendland MF, Tsuruda J, Norman D. Diffusion-weighted MR imaging of anisotropic water diffusion in cat central nervous system. Radiology. 1990; 176:439–445. [PubMed: 2367658]

Moseley ME, Kucharczyk J, Asgari HS, Norman D. Anisotropy in diffusion-weighted MRI. Magn Reson Med. 1991; 19:321–326. [PubMed: 1652674]

Moseley ME, Liu C, Rodriguez S, Brosnan T. Advances in magnetic resonance neuroimaging. Neurol Clin. 2009; 27:1–19. xiii. [PubMed: 19055973]

Otting G, Liepinsh E, Farmer BT 2nd, Wuthrich K. Protein hydration studied with homonuclear 3D 1H NMR experiments. J Biomol NMR. 1991; 1:209–215. [PubMed: 1726782]

Salomir R, DS B, Moonen CTW. A fast calculation method for magnetic field inhomogeneity due to an arbitrary distribution of bulk susceptibility. Concepts in Magnetic Resonance Part B. 2003; 19B:26–34.

Schofield MA, Zhu Y. Fast phase unwrapping algorithm for interferometric applications. Optics Letters. 2003; 28:1194–1196. [PubMed: 12885018]

Schweser F, Deistung A, Lehr BW, Reichenbach JR. Quantitative imaging of intrinsic magnetic tissue properties using MRI signal phase: An approach to in vivo brain iron metabolism? Neuroimage. 2010

Schweser F, Deistung A, Lehr BW, Reichenbach JR. Quantitative imaging of intrinsic magnetic tissue properties using MRI signal phase: an approach to in vivo brain iron metabolism? Neuroimage. 2011a; 54:2789–2807. [PubMed: 21040794]

Schweser F, Deistung A, Lehr BW, Reichenbach JR. Quantitative imaging of intrinsic magnetic tissue properties using MRI signal phase: An approach to in vivo brain iron metabolism? Neuroimage. 2011b; 54:2789–2807. [PubMed: 21040794]

Shmueli K, Li T-Q, Yao B, Fukunaga M, Duyn JH. The contribution of exchange to MRI phase contrast in the human brain. Neuroimage. 2009; 47:S72.

Tuch DS, Reese TG, Wiegell MR, Makris N, Belliveau JW, Wedeen VJ. High angular resolution diffusion imaging reveals intravoxel white matter fiber heterogeneity. Magn Reson Med. 2002; 48:577–582. [PubMed: 12353272]

van Zijl P, Ruessink B, Bulthuis J, MacLean C. NMR of partially aligned liquids: magnetic susceptibility anisotropies and dielectric properties. Accounts of Chemical Research. 1984; 17:172–180.

Wharton S, Bowtell R. Whole-brain susceptibility mapping at high field: A comparison of multiple- and single-orientation methods. Neuroimage. 2010; 53:515–525. [PubMed: 20615474]

Yushkevich PA, Piven J, Hazlett HC, Smith RG, Ho S, Gee JC, Gerig G. User-guided 3D active contour segmentation of anatomical structures: Significantly improved efficiency and reliability. Neuroimage. 2006; 31:1116–1128. [PubMed: 16545965]

Zhong K, Leupold J, von Elverfeldt D, Speck O. The molecular basis for gray and white matter contrast in phase imaging. Neuroimage. 2008; 40:1561–1566. [PubMed: 18353683]

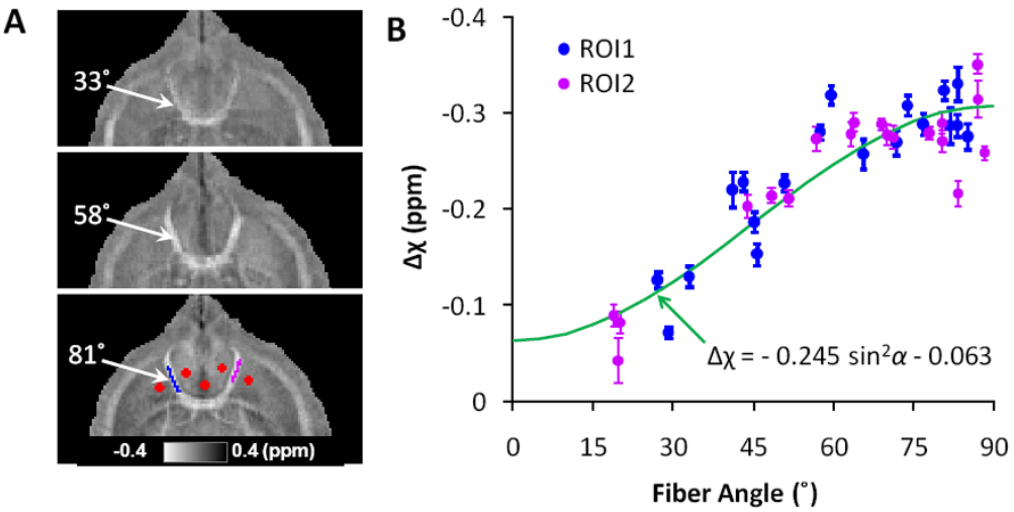

Figure 1.

Orientation dependence of the apparent magnetic susceptibility (AMS). (A) The contrast between gray and white matter depends on the fiber angle. The right limb of the anterior commissure (blue ROI) becomes brighter as the fiber angle increases (arrows). Red circles illustrate ROI in gray matter for susceptibility reference. (B) AMS increases monotonously as the fiber angle decreases following a sine squared relationship. Maximum AMS is achieved when the fiber is aligned with the external field.

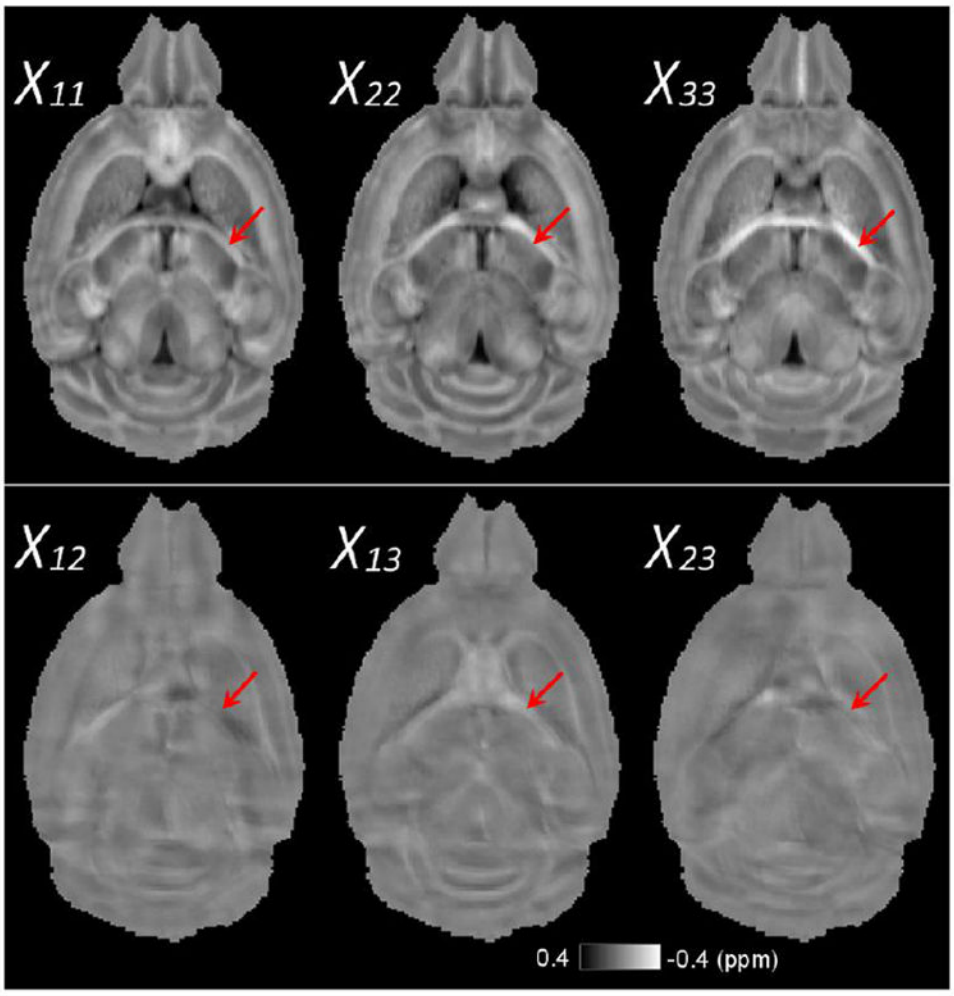

Figure 2.
Elements of susceptibility tensor demonstrating susceptibility anisotropy. The six independent elements of the susceptibility tensor are shown for a representative dorsal slice. Off diagonal terms (χ_{12}, χ_{13} and χ_{23}) are significant only in the white matter. The varying contrast in the hippocampal commissure (red arrows) among the tensor elements demonstrates strong susceptibility anisotropy.

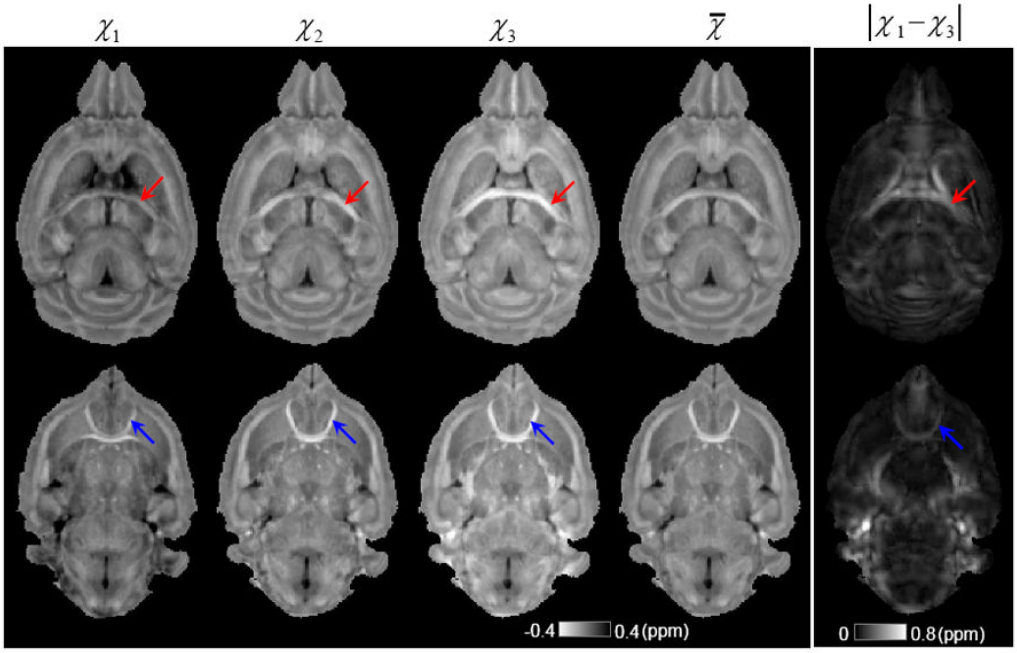

Figure 3.

Principal susceptibility determined by eigenvalue decomposition of two dorsal slices. The three principal susceptibilities vary significantly in the white matter such as the hippocampal commissure (red arrows) and the anterior commissure (blue arrows). The principal susceptibilities are relatively homogeneous in the gray matter. Both principal susceptibilities and mean susceptibility offer excellent contrast between gray and white matter. Hippocampal commissure and anterior commissure are also highlighted in $|\chi_1 - \chi_3|$, which indicated stronger susceptibility anisotropy than gray matter.

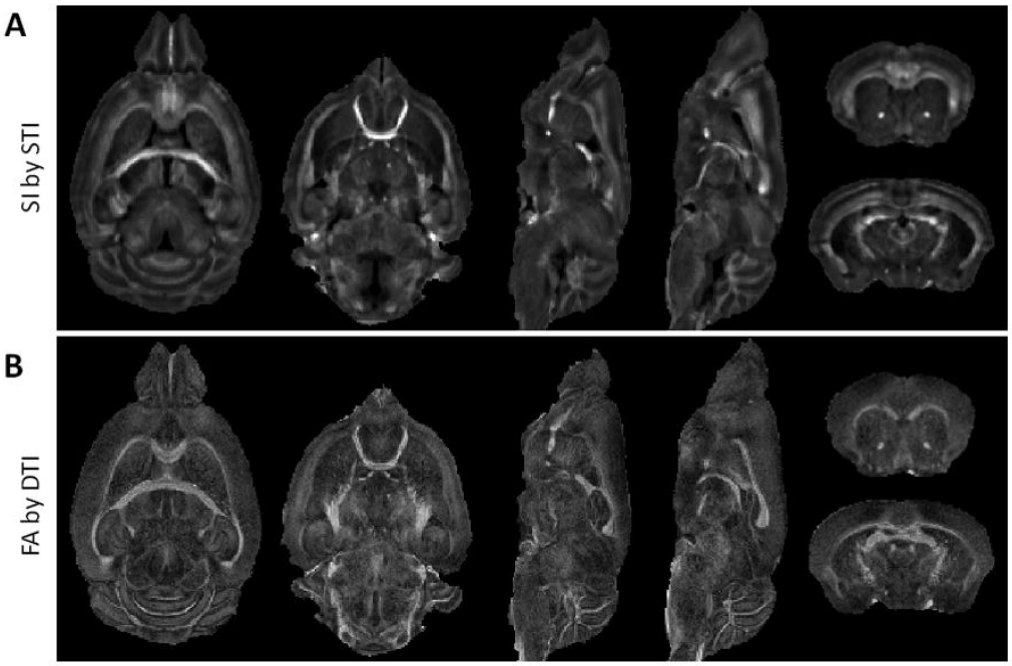

Figure 4.
Susceptibility index (*SI*) compared to DTI diffusion anisotropy (FA). (A) *SI* of representative dorsal, sagittal and coronal slices. (B) Diffusion FA at the same three slices.

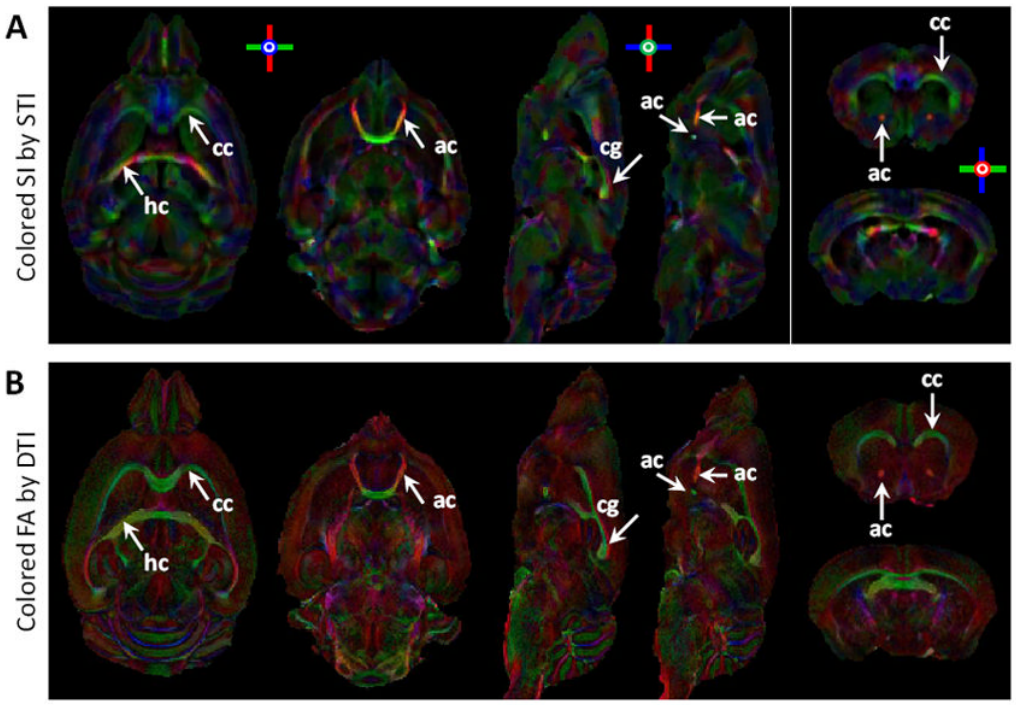

Figure 5.

Comparison of color-coded STI *SI* and DTI FA. Red represents the anterior-posterior direction; green represents the left-right direction; blue represents the dorsal-ventral direction. Overall, the colors in major fiber bundles (arrows) show good consistency while differences are also present. Similar to DTI, STI color maps demonstrate the striking capability of separating fiber bundles in close contact such as the corpus callosum (green) and the cingulum bundle (red) shown in the third column (arrows). Abbreviations: hc – hippocampal commissure; cc – corpus callosum; ac – anterior commissure; cg – cingulum.

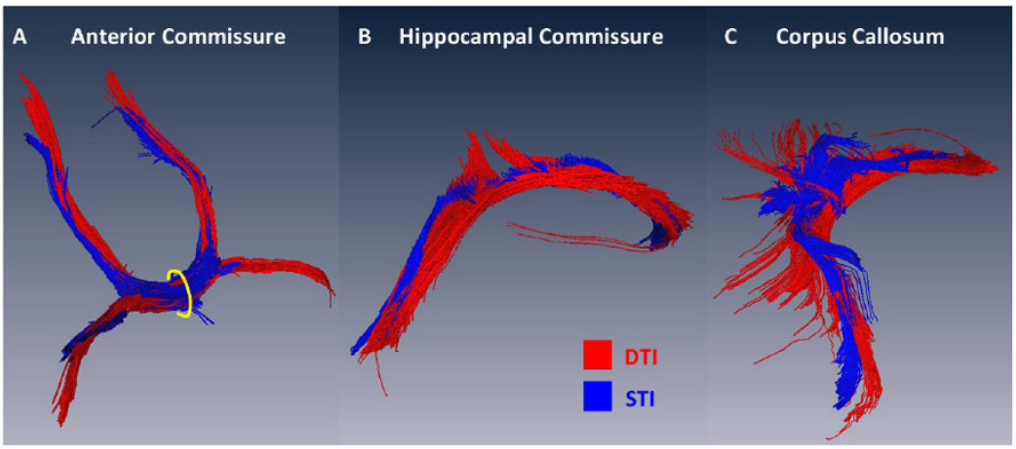

Figure 6.

Comparison of STI and DTI fiber tracts in selected fiber bundles. (A) The anterior commissure; (B) the hippocampal commissure; (C) the posterior corpus callosusm. In general, similar fiber tracts are reconstructed by both techniques while DTI tracts appear to be smoother at the edges of the fiber bundle. In all cases, a single starting ROI was chosen in the middle of each bundle (e.g. the yellow oval in (A)).

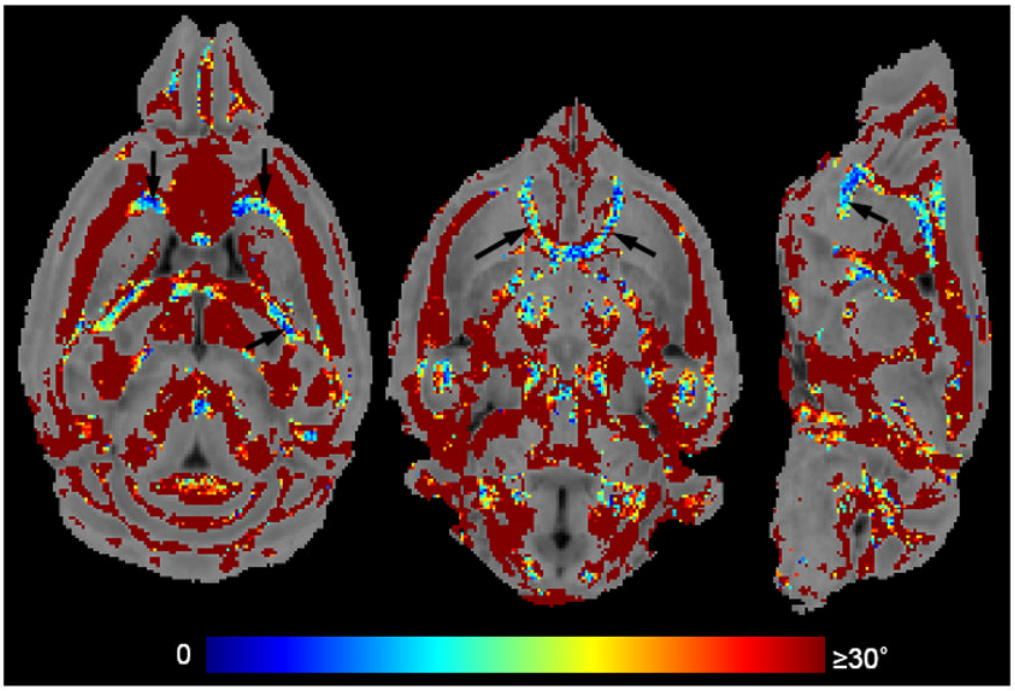

Figure 7.

Angles between the major eigenvectors of STI and DTI in voxels of high SI value. $\bar{\chi}$ was used as the background image for anatomical information. The threshold for SI was 0.2. Three slices are shown from left to right that encompass major fiber bundles (black arrows) including the corpus callosum, the hippocampal commissure and the anterior commissure. The angles between STI and DTI eigenvectors are small in the major fiber bundles while significantly larger in more complex and smaller fiber structures.

Table 1

Fiber statistics obtained with DtiStudio.

	Method	Number of fibers	Average length (mm)	Maximum length (mm)
Anterior commissure	STI	640	2.5	7.8
	DTI	512	3.6	9.1
Hippocampal commissure	STI	1358	1.5	3.0
	DTI	1888	2.9	5.7
Posterior corpus callosum	STI	889	2.9	7.6
	DTI	1175	4.1	9.9